Loss of ULK1 impairs autophagy activation, spheroid viability, and tumor progression in epithelial ovarian cancer

Jack D. Webb
Western University
Lauren Viola
Western University
Adrian Buensuceso
Western University
Matthew J. Borrelli
Western University
Yudith Ramos Valdes
London Health Sciences Centre
Bipradeb Singha
Western University
Trevor G. Shepherd (tshephe6@uwo.ca)
Western University

Research Article

Keywords: Autophagy, ovarian cancer, metastasis, autophagic flux, CRISPR/Cas9, spheroids, xenografts

Posted Date: October 3rd, 2023

DOI: https://doi.org/10.21203/rs.3.rs-3352490/v1

Additional Declarations: No competing interests reported.

Abstract

Introduction: Epithelial ovarian cancer (EOC) remains a leading cause of gynecological cancer-related deaths due its late diagnosis and the absence of effective treatments for chemo-resistant disease. EOC metastasizes through peritoneal dissemination, often forming multicellular spheroids, in which autophagy—a cell survival mechanism—is induced, requiring ULK1 (Unc-51-like kinase 1) activity. Our study aims to further understand the role of ULK1 in EOC tumor growth and metastasis.

Methods: Using CRISPR/Cas9 technology, we ablated the *ULK1* gene in EOC cell lines OVCAR8 and HEYA8, and the fallopian tube derived FT190 control line. Western blotting confirmed ULK1 loss and key autophagy markers. Autophagic flux was assessed using fluorescence microscopy and cell viability by Trypan Blue, Cell Titer-Glo, and Caspase-Glo assays. We tested sensitivity to carboplatin and paclitaxel treatments in cell culture, while bioluminescent imaging monitored tumor progression of xenografts*ULK1*KO. Immunohistochemistry (IHC) was performed to assess Ki67 for cell proliferation and cleaved caspase-3 for apoptosis.

Results: Our results show that ULK1 loss leads to impaired autophagy in EOC spheroids, with reduced LC3 processing and elevated p62 levels. Intriguingly, FT190 cells maintained autophagy which correlated with elevated ULK2 expression. All cell lines lacking *ULK1*KO had reduced spheroid cell viability and spheroid integrity. Surprisingly, ULK1 loss led to differential sensitivity to chemotherapy agents carboplatin and paclitaxel between OVCAR8 and HEYA8 cells. ULK1 deficiency reduced tumor burden in xenografted mice, although differences were observed in tumor growth rate and extent of metastasis between OVCAR8 and HEYA8 cells. Furthermore, Ki67 and cleaved caspase-3 staining revealed reduced cell proliferation and increased apoptosis respectively in tumors derived from *ULK1*KO cells.

Conclusions: ULK1 is required for EOC spheroid formation and cell survival while in suspension likely through its regulation of autophagy, but it may have a lesser role for autophagy regulation in precursor cells. ULK1 deficiency does not increase EOC cell sensitivity to standard-of-care chemotherapy, possibly indicating that other therapeutic strategies would be needed to synergize with autophagy inhibition for EOC treatment.. Altogether, ULK1 may have a multifaceted role in EOC beyond autophagy regulation, by contributing to early dissemination of as spheroids and establishment of secondary tumors

BACKGROUND

Epithelial ovarian cancer (EOC) has the fifth-highest death-to-incidence ratio for all cancers in women. EOCis the leading cause of death from gynecologic cancers due to its late-stage diagnosis and no effective strategies for treating chemo-resistant disease[1]. EOC patients are typically treated with aggressive surgical debulking and cytotoxic carboplatin/paclitaxel combination chemotherapy, yet nearly 80% will relapse with resistant disease in five years[2]. Mechanisms that promote the survival of residual EOC cells following treatment, and the eventual re-growth of resistant disease, are crucial areas of active investigation. EOC spreads by tumor cells disseminating directly into the peritoneal space, often

suspended in ascites, then attaching to serosal surfaces of the abdominal cavity to form secondary deposits3,[4]. Clusters of metastatic EOC cells, known as spheroids, accumulate in the malignant fluid of patients with advanced disease[5]. Spheroids are known to promote metastasis with increased cell survival in the face of chemotherapy and they possess enhanced adhesive and invasive capabilities[6,7]. In addition, we have clearly demonstrated that spheroid cells take on numerous phenotypic changes, such as cellular quiescence[8], epithelial-mesenchymal transition[9], activated stress metabolism[10,11], and autophagy[12], all of which contribute to tumor cell dormancy phenotype of residual disease, and the ultimate emergence of chemo-resistance.

Autophagy acts as a cellular recycling system, helping to dispose of damaged organelles and remove harmful or dysfunctional proteins. At the same time, it replenishes the cell with essential molecules needed for metabolism and other biological pathways[1314,15]. While autophagy is crucial for keeping cells in a balanced state, its role in disease, particularly cancer, is complex and can serve dual purposes. By eliminating damaged and dysregulated cell growth proteins, autophagy may contribute to tumor suppression by functioning as a brake for proliferation[16]. For example, autophagy has been shown to activate p53-mediated cellular senescence through the degradation of an inhibitory p53 isoform[17]. Despite suppression of autophagy during early tumorigenesis, autophagy seems to be upregulated during later stages as protective mechanism against stressful metabolic conditions imposed during growth and metastasis[18]. During hypoxia, oxygen consumption is reduced thorough autophagy-dependant degradation of mitochondria to maintain cell viability[19]. Additionally, autophagy can prevent apoptosis-deficient cells from undergoing necrosis, exacerbating inflammation and tumor growth[20]. Cancer cells also activate autophagy and confer resistance to chemotherapy and radiation[21,22].

Autophagy induction is controlled by the Unc-51-like kinase (ULK) complex, which consists of ULK1/2, autophagy-related gene 13 (ATG13), and focal adhesion kinase interacting protein (FIP200) that initiates formation of phagophores[23]. ULK1 is a serine- threonine kinase that integrates upstream signals from nutrient sensors to either activate or repress autophagy. In nutrient rich conditions, the mammalian target of rapamycin (mTOR)/PI3K pathway suppresses autophagy by inactivating the ULK complex and preventing phagophore formation[24,25]. Under metabolic stress, mTORC1 kinase activity is inhibited and de-represses the ULK1 complex[26], activating autophagy and phagophore formation. Additionally, the ULK1 complexed is directly activated by AMP-activated protein kinase (AMPK) to initiate autophagy[27] .

We have previously demonstrated a coordinated response AMPK activation[10] and AKT-mTORC1 downregulation[28] in HGSOC spheroids. We have also shown that EOC spheroids have increased ULK1 expression which parallels autophagy induction, and that transient knockdown and inhibitor treatments *in vitro* results in a block in autophagy and reduced cell viability[29]. Given the persistent challenges of late-stage diagnosis and chemo-resistance in EOC patients, we sought to exploit the therapeutic vulnerabilities associated with autophagy and the ULK1 complex. Leveraging our insights from prior work

on autophagy in EOC spheroids and utilizing CRISPR/CAS9 technology for ULK1 ablation, we aim to elucidate ULK1's role as a potential therapeutic target in EOC metastasis.

METHODS

Cultured cell lines.

The cell lines OVCAR8, OVCAR8-*ULK1*KO, HeyA8, and HeyA8-*ULK1*KO were grown in RPMI-1640 medium (Wisent), while FT190 and FT190-*ULK1*KO were grown in DMEM/F12 medium (Life Technologies). All growth media were enhanced with 10% fetal bovine serum. The OVCAR8 and HeyA8 cells were procured from the American Type Culture Collection. Adherent cells were sustained on tissue culture-treated polystyrene (Sarstedt, Newton, NC, USA), and spheroids were kept in Ultra-Low Attachment (ULA) cluster plates (Corning, NY, USA). The immortalized human fallopian tube secretory epithelial cell line FT190 (cite) was generously provided by R. Drapkin from the University of Pennsylvania, Philadelphia, PA. The Centre for Applied Genomics (The Hospital for Sick Children, Toronto, ON, Canada) authenticated all cell lines through short tandem repeat analysis and routinely examined them for mycoplasma using the Universal Mycoplasma Detection Kit (30-1012K; ATCC).

Generation of ULK1 KO cell lines:

CRISPR/Cas9 (Santa Cruz Technology, sc-400516-KO-2 Lot# C3016) was used to ablate ULK1 gene expression in OVCAR8, HEYA8, and FT190 cells. Briefly, cells were seeded at 100-150k per well of a 6-well plate and transfected the following day. Cells were lifted four days post-transfection and sorted using fluorescence activate cell sorting (FACS) into 96-well plates. Clones were left to grow for a minimum of two weeks, where colony formation was subsequently observed. Colonies were harvested and plated into 6-well plates, and then 10cm plates upon reaching confluency. Cells were harvested for protein lysates and screening for ULK1 loss via western blot and passaged for continued culturing and subsequent pooling of clones.

Generation of Nuclight GFP cell lines:

Cells were transduced with Incucyte® Nuclight Green Lentivirus (EF1a, Puro) (Sartorius, #4624) following the manufacturer's instructions. After transduction, cells were cultured in complete media supplemented with puromycin to select for successfully transduced cells. The transduced and puromycin-selected cell population was subjected to fluorescence-activated cell sorting (FACS) to isolate GFP (green fluorescent protein) -positive cells. The isolated GFP + cells were then expanded and used for further analysis or experimentation.

Generation of mCherry-eGFP-LC3 cell lines:

Parental and *ULK1*KO cells were transfected using an mCherry-eGFP-LC3B autophagy reporter plasmid (Addgene, #22418). After transfection, cells were grown in complete media containing G-418 for two weeks to select those with successful reporter plasmid integration. Following the selection phase, the

cells were cultured in complete media without G-418 for another four weeks, allowing for growth and recovery. Cells were then sorted using FACS to identify double positive cells (GFP+, mCherry+).

Generation of luc2tdTomato cell lines:

Cells were transduced with pCDH-EF1-Luc2-P2A-tdTomato (plasmid #72486, Addgene) following the manufacturers instructions. After transduction, cells were subjected to FACS to isolate tdTomato + cells. Cells were cultured in complete media for growth and recovery. Cells were then subjected to another round of FACS to select cells varying intensities of tdTomato expression.

Antibodies and reagents:

Antibodies against ULK1 (#8054S, 1:1000), p62 (#5114S, 1:1000), LC3B (#2775S, 1:1000), p-Beclin1 (#5410S), and Beclin1 (#3738S) were purchased from Cell Signaling Technology. Anti-ULK2 antibody (AB97695, 1:1000), ATG16L1 (AB187671), p-ATG16L1 S30 (AB19016, 1:100), and mCherry (AB167453, 1:500) was purchased from Abcam. Anti-actin antibody (A2066, 1:25000) was purchased from Millipore. Antibody against tubulin (T5168; 1:40000) was purchased from Sigma. HRP-conjugated antibodies against mouse IgG (NA931; 1:10000) and rabbit IgG (NA934; 1:10000) were purchased from GE Healthcare. All antibodies were diluted in tris-buffered saline-Tween 20 containing 5% bovine serum albumin.

Immunoblot analysis:

The Bio-Rad Mini-PROTEAN II Electrophoresis System was employed for immunoblotting following the manufacturer's guidelines, utilizing in-house prepared gels (30% acrylamide/bis solution 37.5:1, catalog number 1610158; Bio-Rad). Densitometric analysis was conducted using the Image Lab 6.05 software suite (Bio-Rad).

Preparation of wholecell lysates:

For assessment of all proteins, 4, 8, 24, 48, 72-hour whole-cell lysates were generated from adherent cells cultured at a density of 0.75-1× 10^6 cells in 10 mL medium (10 cm dish), or spheroid cells cultured at a density of 1–3× 10^6 cells in 15 mL medium (35 mm ULA well). Seeding numbers were chosen to obtain acceptable protein yields for each cell line.

Wholecell lysates. Adherent cells cultivated on tissue culture-treated plates or dishes were gathered by removing the medium, washing twice with cold PBS, and then scraping into a modified RIPA buffer. Spheroids (a minimum of 1.5 × 10^6 cells per sample) were collected by transferring the cell suspension into an ice-cold conical tube, followed by centrifugation using a swinging bucket rotor (800 × g at 4°C for 4 minutes) to form a pellet. The medium was then aspirated, and the pellet was resuspended in at least 10 mL of cold PBS. This process was repeated by resuspending the pellet in cold PBS once more, followed by centrifugation and aspiration of the PBS. The resulting cell pellets were lysed using modified RIPA buffer, vortexed, exposed to one freeze-thaw cycle, and finally clarified through centrifugation (maximum × g at 4°C for 20 minutes).

Microscopy:

Brightfield images of spheroids seeded in 24-well ULA plates were captured using a Leica DMI4000B inverted microscope. Immunofluorescent images of mCherry-eGFP-LC3 and Nuclight GFP spheroids were captured using an IncuCyte S3 Live-Cell Analysis System (Sartorius).

Spheroid viability assays.

For bulk spheroids. Cells were placed in 24-well ultra-low attachment (ULA) cluster plates at a density of 0.5-1 × 10^5 cells per well in 1 mL of medium. Spheroids were then gathered into chilled microcentrifuge tubes and centrifuged at 500×g for 3 minutes to form pellets. After aspirating the medium, the pellets were washed with 500 µL of PBS (avoiding cell uptake into the pipette tip), centrifuged once more as previously described, and resuspended in 50–250 µL of trypsin/EDTA. The suspension was incubated at 37°C with periodic gentle agitation every 10 minutes until no aggregates were visible (10–30 minutes). Trypsin was inactivated by adding an equal volume of FBS, followed by the addition of Trypan Blue dye (in a volume equal to the combined trypsin/EDTA and FBS), and gentle mixing via pipetting. Cell counting was carried out using a TC20 Automated Cell Counter (Bio-Rad).

For single spheroids. Cells were seeded in a 96-well round bottom ULA plate at a density of 2000 cells per well in 100 µL of medium. For alamarBlue assays, cells were incubated with a final dilution of 1:10 for 4, 24, or 48-hours and fluorescence was measured using a Biotek plate reader. For CellTiter-Glo (Promega, G7572) and Caspase-Glo 3/7 (Promega, G8092) Assay's, 100 µL of reagent was added and the plate was frozen at -80°C. After 24-hours, plates were incubated in the dark for 60 min on a plate rocker. Wells were transferred to a 96-well opaque white plate and luminescence was read on a Biotek plate reader.

Doubling time:

Cells expressing Nuclight GFP were placed in 96-well standard-well ultra-low attachment (ULA) cluster plates at a density of 0.5-1 × 10^5 cells per well in 200 µL of medium. Fluorescent images were captured at 4-hour intervals in the IncuCyte S3 Live-Cell Analysis System (Sartorius). Growth curves and doubling time calculations were generated in GraphPad Prism 9. Adherent and spheroid doubling time calculations were completed using the Green Object Count and Green Mean Intensity feature, respectively.

Carboplatin and paclitaxel treatments:

Paclitaxel (5mM in DMSO) was purchased from Cayman Chemical Company (10461) and stored at -20°C. Carboplatin (27mM in saline) was received from the London Regional Cancer Program and stored at 4°C.

To determine adherent carboplatin and paclitaxel IC_{50} values, 2000 cells in 100 µL media were seeded in a 96-well plate. The next day, cells were treated individually over a 12-point concentration gradient. After 72 hours of treatment, cell viability was determined using the alamarBlue Cell Viability Reagent (Invitrogen CAT# DAL 1025) according to the manufacturer's instructions. To determine spheroid

carboplatin and paclitaxel C_{50}values, 2000 cells in 100 µL media were seeded in a 96-well ULA plate to induce spheroid formation. After 72-hours, cells were treated individually over a 12-point concentration gradient for an additional 72-hours. Following treatment, viability was determined by alamarBlue viability assay. Viability was assessed 4- and 48-hours post alamarBlue incubation for carboplatin and paclitaxel, respectively. IC50 values were calculated using GraphPad Prism 9.

Xenotransplantation assays:

NOD/SCID female mice (8–10 weeks old; Charles River Laboratories) were inoculated by intraperitoneal injection with 150 µL of PBS containing the following numbers of cells: OVCAR8/OVCAR8-*ULK1*KO, 2 × 10^6; HeyA8/HeyA8-*ULK1*KO, 1 × 10^6). For survival analyses (OVCAR8, OVCAR8-*ULK1*KO, HeyA8, HeyA8-*ULK1*KO cells), mice were monitored daily after intraperitoneal injection and euthanized using standard criteria for humane endpoints (i.e., lethargy, hunched posture, impaired breathing, extreme weight loss, excessive ascites). Mice received weekly injections of D-luciferin (Perkin Elmer, #122799) at 75mg/kg in 100µL of PBS to monitor tumor progression via bioluminescent imaging using our IVIS Lumina S5 system. Mice were provided chow (Envigo, #2919) and water *ad libitum* throughout the study. All animal experiments were approved by Institutional Animal Care and Use Committee of the University of Western Ontario (London, Ontario, Canada) and carried out in accordance with the approved guidelines.

IHC quantification and scoring

IHC analysis was performed using the Fiji distribution of ImageJ[30]. Ki67-positive nuclei were masked using the Trainable Weka Segmentation plugin[31], and masked regions were counted using a minimum particle area of 120 pixels. Cleaved caspase-3 staining in xenograft tumor sections was evaluated using the “IHC Profiler” plugin for ImageJ as described previously[32]. Positive caspase-3 staining reflects “high-positive” and “positive” as defined by IHC profiler.

Statistical analysis:

Statistical analyses were performed using GraphPad Prism 9 (GraphPad Software). Specific analysis details are described in figure legends.

RESULTS

ULK1 is required for autophagy activation in EOC spheroids

Autophagy ensures homeostasis during challenging conditions by facilitating the degradation of intracellular components and subsequent replenishment of vital biomolecules. Induction of autophagy is controlled by the ULK complex, notably ULK1. Our prior investigations revealed elevated ULK1 expression in EOC spheroids, which corresponded with heightened autophagy activation. To further elucidate the role of ULK1 on autophagy activation, we ablated ULK1 in EOC cells using CRISPR/Cas9 and subsequently pooled multiple independent clones to generate a population of ULK1 knockout (*ULK1*KO) cells. Upon examining OVCAR8 and HEYA8 spheroids, we observed increased ULK1 expression in parental spheroids,

while *ULK1*KO cells exhibited a distinct absence of ULK1 (Fig. 1A). To assess the influence of ULK1 loss on autophagy, we examined crucial proteins involved in the autophagic pathway. Notably, p62 accumulation serves as an indicator of autophagy inhibition, while its decrease suggests autophagy induction[33]. Meanwhile, the LC3II:I ratio, derived from the processing of LC3I to LC3II—a marker of autophagosome membranes—reflects autophagy activation[34]. In both OVCAR8 and HEYA8 *ULK1*KO day 3 spheroids, we detected a significant increase in p62 expression and a substantial reduction in LC3II:I compared to their parental cell lines (Fig. 1B). These findings were recapitulated under serum starvation conditions in adherent cells (Supplemental Fig. 3). Significant decreases in the LC3II:I ratio can be observed as early as 4 hours within spheroids (Fig. 2B/D). Intriguingly, ULK1 loss resulted in a marked elevation of LC3I under adherent conditions (Supplemental Fig. 2). Additionally, we verified the abrogation of ULK1 activity through its direct downstream substrate, p-Beclin1 (S30). As anticipated, ULK1 loss eliminated ULK1 activity in EOC spheroids (Fig. 1B). We also sought to evaluate the autophagic flux, defined as the efficiency and rate at which cellular components are degraded and recycled through the autophagy pathway[29]. To accomplish this, we generated EOC parental and *ULK1*KO cells expressing the mCherry-eGFP-LC3B autophagy reporter. Upon exposure to the acidic lysosome environment, GFP fluorescence is quenched due to its sensitivity to acidic conditions, whereas mCherry fluorescence remains stable. As a result, quantifying monomeric mCherry expression via Western blot analysis and the mCherry/GFP ratio through immunofluorescence imaging serves as a reliable indicator of autophagic flux. To clarify whether this role for ULK1 was specific to spheroids, we first exposed EOC cells to serum deprivation in an adherent setting, which is an established robust inducer of autophagy[30]. We noted a considerable attenuation in monomeric mCherry and an increase in p62 levels in OVCAR8 *ULK1*KO cells under serum starved conditions compared to the parental cells (Supplemental Fig. 3). In HEYA8 *ULK1*KO cells, we observed significant increases in p62 and decreases in the LC3II:I. Interestingly, no changes in monomeric mCherry levels were seen 24 hours post serum starvation (Supplemental Fig. 3). However, under basal conditions in spheroids, significant reductions in the mCherry:RFP can be observed starting at 120 hours, while such reductions in OVCAR8 *ULK1*KO spheroids were evident as early as 48 hours (Fig. 1D). These findings indicate that the autophagic flux is notably impaired in EOC *ULK1*KO cells. Collectively, these results indicate that ULK1 is essential for autophagy activation in EOC spheroids.

Viability is significantly impaired in EOC ULK1 KO spheroids

The assessment of ULK1 and autophagy during spheroid formation was crucial, as spheroids provide enhanced viability and protection to EOC cells from chemotherapeutic damage[35]. To further understand how ULK1 and autophagy contribute to spheroid formation and viability, *ULK1*KO cells were grown in suspension culture and viability was assessed over time. We observed notable differences in morphology, density, cell number, and integrity in HEYA8 *ULK1*KO bulk spheroids compared to the parental spheroids, while OVCAR8 *ULK1*KO spheroids retained their morphology but displayed differences in cell number (Fig. 3A). The Trypan blue exclusion assay was conducted on spheroids for multiple days to quantitatively evaluate viable cell counts, which showed a decline in viable cells over time. A significant reduction in viable cells was observed in OVCAR8 and HEYA8 *ULK1*KO spheroids by day 3 and 10,

respectively (Fig. 3B). To determine the cause of the decreased viability in *ULK1*KO spheroids, we investigated whether it was due to decreased proliferation or increased apoptosis. To evaluate cell proliferation, we generated EOC parental and *ULK1*KO cells that expressed nuclear-localized GFP, enabling fluorescence imaging via the Incucyte Live-cell analysis system. No growth rate disparities were observed between EOC parental and *ULK1*KO spheroids (Fig. 3D). Additionally, we conducted Cell-Titer Glo assays as an alternative method to indirectly measure cell growth and discovered no significant differences in this analysis as well (Fig. 3E). We employed the Caspase-Glo 3/7 assay to assess the activity of caspase-3 and − 7 in apoptotic spheroids, observing substantial increases in *ULK1*KO spheroids (Fig. 3E). Thus, it seems that ULK1 plays a crucial role in sustaining the viability of EOC spheroids.

ULK1 is not required for autophagy activation in EOC precursor spheroids

Emerging evidence has shifted the paradigm regarding the origin of HGSOC, suggesting that the majority arise from the fallopian tube rather than the previously believed ovarian surface epithelial cells[36]. Given that autophagy has been identified as potentially tumor-suppressive, it became imperative for us to investigate the role of ULK1 on autophagy specifically in these fallopian tube-derived cells. We observed significant decreases in ULK1 activity via p-Beclin1 (S30) (Fig. 4B), however, no significant differences in p62 expression and LC3II:I ratios were observed between FT190 parental and *ULK1*KO spheroids (Fig. 4B). To address potential compensation due to ULK1 loss, we investigated ULK2 protein expression, a homolog of ULK1 believed to be redundant in autophagy activation[37]. We noticed a substantial increase in ULK2 expression under adherent conditions (Fig. 4B); however, in *ULK1*KO spheroids, ULK2 activity could be compensating to initiate autophagy. We evaluated the viability of FT190 *ULK1*KO spheroids and observed reduced spheroid integrity (Fig. 4E) and a significant reduction in the number of viable cells (Fig. 4F), likely due to the induction of apoptosis (Fig. 4H). Although there are fewer viable cells, there seems to be a higher proportion of metabolically active cells, as suggested by the CellTiter-Glo assay (Fig. 4H).

ULK1 affects both initial and advanced phases of tumor development in xenograft models

HGSOC exhibits a distinct metastatic pattern in that cells from the fallopian tube and primary tumor site are directly shed into the peritoneal cavity, aggregating into spheroid clusters. This leads to fluid build-up in the peritoneal cavity, further aiding the spread of these spheroids[2,4]. Considering our data highlighting ULK1's role in autophagy activation and spheroid viability, we aimed to evaluate the necessity of ULK1 for EOC tumor formation and metastasis in xenograft models. To accomplish this, we generated both parental and *ULK1*KO cells that express luciferase, enabling BLI measurements to track and quantify tumor development. These cells were injected intraperitoneally (i.p.) into female NOD/SCID mice, and tumor progression was monitored over time. ULK1 deficiency in OVCAR8 cells led to a reduction in tumor burden at all time points, with significant decreases observed during mid-to-late stage of disease

progression (Fig. 5A/B). In contrast, HEYA8 *ULK1*KO cells exhibited a significant decrease in tumor burden during the early stage of disease progression (Fig. 5D/E). The overall survival rate increased and decreased for mice injected with OVCAR8 and HEYA8 *ULK1*KO cells, respectively (Fig. 5C/G). Minimal differences in average survival time were seen. Intriguingly, loss of ULK1 in EOC cells resulted in fewer tumors across several metastatic sites, with notable decreases in ascites formation and abdominal and omental tumors (Fig. 5D/H). When ascites-derived cells were cultured under spheroid conditions, we observed elevated levels of p62 and LC3I (Fig. 6D). Moreover, these cells showed a significant decrease in the LC3II:I ratio and a suppression of ULK1 activity, as evidenced by alterations in Beclin1 S30 levels (Fig. 6D). These findings point to compromised autophagy activation. To further elucidate the role of ULK1 in tumor cell proliferation and apoptosis, we utilized immunohistochemistry analysis of tumor tissues. OVCAR8 *ULK1*KO tumor samples showed a higher proportion of Ki67-positive nuclei (Fig. 6B) despite a reduced total number of Ki67-positive nuclei. In contrast, HEYA8 *ULK1*KO tumors demonstrated a lower proportion of Ki67-positive nuclei (Fig. 6B), while no differences in total number of Ki67-positive nuclei were seen. OVCAR8 *ULK1*KO tumors exhibited more pronounced staining for cleaved caspase 3 (Fig. 6C), a well-established marker for apoptosis, pointing towards enhanced cell death in these tumors. On the other hand, HEYA8 *ULK1*KO tumors did not show any remarkable differences in cleaved caspase 3 staining (Fig. 6C). Nonetheless, it seems that ULK1 has a crucial function in both initial and advanced phases of EOC tumor cell spread.

DISCUSSION

To our understanding, we are the first to show the crucial role of ULK1 for autophagy using both *in vitro* and *in vivo* models of EOC metastasis. Our results show that ULK1 is essential for activating autophagy in EOC spheroids, and that ULK1 deficiency hinders autophagic flux thereby reducing spheroid cell viability. Furthermore, our tumor xenograft models of disseminated EOC indicate that ULK1 is crucial in both early and advanced stages of tumor spread.

The function of ULK1 as a central regulator of autophagy initiation is well established in existing literature[38]. In our study, the observed increase in ULK1 protein expression in OVCAR8 and HEYA8 parental cells is consistent with autophagy activation, as indicated by the significant rise in the LC3II:I ratio. In contrast, the unaltered LC3II:I ratio and elevated p62 levels in *ULK1*KO spheroids indicate compromised autophagy activation. Intriguingly, the loss of ULK1 did not hinder autophagy activation in FT190 precursor cells. Substantial increases in ULK2 protein expression in FT190 *ULK1*KO cells imply compensatory autophagy activation due to the loss of ULK1, while this was not observed in EOC cells lacking ULK1. This result aligns with one study that reported no alterations in ULK2 expression due to ULK1 inhibition in HGSOC cells [39]; however, that study did not assess high-grade serous ovarian cancer precursor cells. This observation emphasizes that the major requirement for ULK1 on autophagy activation could be specific to malignant cells.

To verify the loss of ULK1 activity, we interrogated protein levels of ATG16L1 and Beclin-1, direct downstream targets of ULK1 known to play pivotal roles in the autophagic process [40]. ATG16L1 is part of

a complex that aids in the conjugation of LC3I to phosphatidylethanolamine (PE), transforming it into LC3II, which then associates with autophagosome membranes[41, 42]. The observed decrease in ULK1-specific p-ATG16L1 (S278) levels in OVCAR8 *ULK1*KO and significant increases of LC3I imply a direct role of ULK1 in LC3 processing and autophagy activation. Moreover, it has been demonstrated that ULK1 activity promotes autophagosomal fusion with lysosomes, supporting our data on impaired autophagic flux [43]. Beclin-1 is another critical element of the autophagy machinery via its role in assembling autophagosomes. ULK1 phosphorylates Beclin-1 at S30, fostering the formation of the VPS34 complex, which is vital for autophagosome nucleation[44, 45]. Indeed, we observed a dramatic ablation of p-Beclin-1 (S30) levels in *ULK1*KO cells compared with parental cell lines confirming the lack of ULK1 activity. Nevertheless, it is essential to mention that our previous findings have shown that Beclin-1 is not required for autophagy activation in EOC spheroids [46]. Thus, herein we used p-Beclin (S30) as a genuine ULK1 substrate rather than imply it mediates ULK1 function in EOC spheroids.

The upregulation of autophagy during cancer progression is known to protect cancer cells from bioenergetic stress and metabolic challenges, as well as to promote chemoresistance [47, 4849]. Given this, investigating ULK1 function in EOC spheroid cell viability is crucial to understanding the complex interplay between autophagy and metastatic progression in this disease. As expected, the loss of ULK1 led to a significant reduction in the number of viable EOC cells over time, emphasizing the importance of ULK1 in promoting EOC spheroid viability. ULK1 has reported functions in both cell cycle progression[50] and in the regulation of apoptosis[51] and therefore sought to evaluate the consequences of ULK1 loss in these contexts. Despite various methods to interrogate proliferation, we observed little evidence that the decrease in cell viability was attributed to alterations in cell proliferation. However, increased apoptotic activity was observed in *ULK1*KO spheroids, indicating that ULK1 may have a role in regulating apoptosis to maintain cell viability in EOC spheroids. ULK1 has been shown to be a key regulator of necrosis-mediated cell death through regulation of RIPK1 [52], possibly contributing to reduced *ULK1*KO cell viability, too.

Our xenograft and immunohistochemistry experiments collectively highlight ULK1's pivotal role in the progression of EOC. We observed a significant decrease in both early and advanced stage tumor cell spread upon ULK1 ablation, along with fewer tumors at metastatic sites and reduced ascites formation. Our *in vitro* experiments also displayed significant reductions in spheroid cell viability across extended time points. Interestingly, this suppression of disseminated disease throughout the peritoneum was accompanied by more tumors appearing to localize to the ovaries. Perhaps tumor establishment in the peritoneal cavity has underlying differences in the requirement for EOC cells to retain functional ULK1 and autophagy activities at new secondary sites during metastasis.

ULK1 in cancer development has demonstrated context-specific functions, particularly among disparate malignancies. For instance, ULK1 depletion significantly reduces tumor growth in hepatocellular carcinoma, as evidenced in both *in vitro* and *in vivo* investigations[53,54]. In contrast, the absence of ULK1 in breast cancer models has been linked to an increased likelihood of osseous metastasis[55]. Here, we

observed contrasting effects on cell proliferation and apoptosis among tumor specimens from the two EOC cell line models. Specifically, OVCAR8 *ULK1*KO samples showed increased rates of both proliferation and apoptosis, whereas HEYA8 *ULK1*KO specimens exhibited decreased proliferation. These differential effects on cell proliferation were not observed *in vitro*, suggesting the direct influence of the tumor microenvironment or other *in vivo* factors. These two EOC cell lines possess inherent differences in gene mutation, notably the presence of mutant p53 in OVCAR8 cells yet HEYA8 cells are *TP53* wildtype These findings highlight ULK1's critical role in tumor growth, dissemination, and survival, making it a potential target for future therapeutic strategies.

Elevated autophagy levels have been associated with unfavorable prognostic outcomes in patients, potentially serving as a mechanism for multi-drug resistance in cancer therapy. Furthermore, *ULK1* mRNA overexpression has been specifically correlated with diminished survival rates in individuals diagnosed with advanced-stage ovarian cancer[29]. Thus, we hypothesized that ULK1 inhibition could potentially enhance the sensitivity of EOC cells to standard-of-care chemotherapy and attenuate disease progression in xenograft models. Intriguingly, we found that ULK1 loss did not synergize with standard-of-care chemotherapeutics, yet in some instances we observed antagonistic effects. This contrasts the results from another group, where ULK1 ablation in OVCAR8 cells sensitized to both carboplatin and paclitaxel in adherent culture conditions[56]. Here, we used an alternative cell viability indicator for both adherent and spheroid conditions, allowing us to quantitatively assess viability and proliferative status in both culture models. Even though extensive research has underscored the role of autophagy in facilitating chemoresistance, and the potential benefits of autophagy inhibition in enhancing chemotherapeutic outcomes[57], our findings suggest that the inhibition of autophagy may counteract the efficacy of standard-of-care chemotherapeutics employed in EOC patient treatment.

CONCLUSIONS

Our research highlights the importance of ULK1 in autophagy activation, spheroid survival, and tumor progression in EOC cells. The functional consequences of ULK1 loss on autophagy and spheroid viability emphasize the potential of targeting ULK1 for therapeutic purposes in EOC treatment. Future research should aim to explore autophagy-dependent and -independent roles of ULK1 in EOC cells which could highlight additional therapeutic targets, as well as examine the potential advantages of combining ULK1 inhibitors with current chemotherapeutic regimens to enhance treatment efficacy.

Abbreviations

EOC
Epithelial ovarian cancer
ULK1
Unc51-like kinase
ATG13
Autophagy-related gene 13

FIP200
focal adhesion kinase interacting protein 200
mTOR
Mammalian target of rapamycin
AMPK
AMP-activated protein kinase
HGSOC
High-grade serous ovarian carcinoma
FACS
Fluorescence-activated cell sorting
GFP
Green fluorescent protein
ULA
Ultra-low attachment
IHC
Immunohistochemistry

Declarations

Ethics approval and consent to participate

All animal experiments were approved by Institutional Animal Care and Use Committee of the University of Western Ontario (London, Ontario, Canada) and carried out in accordance with the approved guidelines.

Consent for publication

Not applicable

Availability of data and materials

All data generated or analysed during this study are included in this published article and its supplementary information files.

Competing interests

The authors declare that they have no competing interests.

Funding

We acknowledge funding support from the Cancer Research Society to TGS, and London Health Sciences Foundation through donations to the Mary & John Knight Translational Ovarian Cancer Research Unit.

JDW was supported by an Obstetrics & Gynaecology Graduate Scholarship from the Department of Obstetrics & Gynaecology at Western University.

Authors' contributions

JDW and TGS conceptualized and designed the study. JDW, LV, YRV, and AB acquired the data. TGS supervised and obtained the funding for the study. BS, MB, and YRV provided additional resources. JDW wrote the original draft of the manuscript and TGS edited the manuscript. All authors read and approved the final manuscript.

Acknowledgements

We are grateful to Ronny Drapkin for providing the FT190 cell line. We are also very grateful to the many donors to the Mary and John Knight Translational Ovarian Cancer Research Unit through the London Health Sciences Foundation for additional infrastructure funding, including the Leica DMI 400B inverted microscope, Bio-Rad Chemidoc, IncuCyte S3, and IVIS Lumina imaging system used in this study.

References

1. Brenner DR, et al. Projected estimates of cancer in Canada in 2020. CMAJ. 2020;192:199–205.
2. Lheureux S, Gourley C, Vergote I, Oza AM. Epithelial ovarian cancer. The Lancet. 2019;393:1240–53.
3. Bowtell DD, et al. Rethinking ovarian cancer II: reducing mortality from high-grade serous ovarian cancer. Nat Publishing Group www Nat com/reviews/cancer. 2015. 10.1038/nrc4019.
4. Lengyel E, et al. Epithelial ovarian cancer experimental models. Oncogene. 2014;33:3619–33.
5. Naora H, Montell DJ. Ovarian cancer metastasis: Integrating insights from disparate model organisms. *Nature Reviews Cancer* vol. 5 355–366 Preprint at https://doi.org/10.1038/nrc1611 (2005).
6. Shield K, Ackland ML, Ahmed N, Rice GE. Multicellular spheroids in ovarian cancer metastases: Biology and pathology. *Gynecologic Oncology* vol. 113 143–148 Preprint at https://doi.org/10.1016/j.ygyno.2008.11.032 (2009).
7. Iwanicki MP et al. ovarian cancer spheroids Use Myosin-Generated Force to clear the Mesothelium. 10.1158/2159-8274.CD-11-0010.
8. Correa RJM, Peart T, Valdes YR, Dimattia GE, Shepherd TG. Modulation of AKT activity is associated with reversible dormancy in ascites-derived epithelial ovarian cancer spheroids. Carcinogenesis. 2012;33:49–58.
9. Rafehi S, et al. TGFβ signaling regulates Epithelial-mesenchymal plasticity in ovarian cancer ascites-derived spheroids. Endocr Relat Cancer. 2016;23:147–59.
10. Peart T. *Intact LKB1 activity is required for survival of dormant ovarian cancer spheroids*. .

11. Buensuceso A, Ramos-Valdes Y, Di Mattia GE, Shepherd TG. AMPK-independent LKB1 activity is required for efficient epithelial ovarian cancer metastasis. Mol Cancer Res. 2020;18:488–500.
12. Correa RJM, et al. Combination of AKT inhibition with autophagy blockade effectively reduces ascites-derived ovarian cancer cell viability. Carcinogenesis. 2014;35:1951–61.
13. Mizushima N, Levine B, Cuervo AM, Klionsky DJ. Autophagy fights disease through cellular self-digestion. *Nature* vol. 451 1069–1075 Preprint at https://doi.org/10.1038/nature06639 (2008).
14. Levine B, Kroemer G. Autophagy in the Pathogenesis of Disease. *Cell* vol. 132 27–42 Preprint at https://doi.org/10.1016/j.cell.2007.12.018 (2008).
15. Leone RD, Amaravadi RK, Autophagy. A targetable linchpin of cancer cell metabolism. *Trends in Endocrinology and Metabolism* vol. 24 209–217 Preprint at https://doi.org/10.1016/j.tem.2013.01.008 (2013).
16. Qu X, et al. Promotion of tumorigenesis by heterozygous disruption of the beclin 1 autophagy gene. J Clin Invest. 2003;112:1809–20.
17. Kwon Y, Kim JW, Jeoung JA, Kim MS, Kang C. Autophagy is pro-senescence when seen in close-up, but anti-senescence in long-shot. *Molecules and Cells* vol. 40 607–612 Preprint at https://doi.org/10.14348/molcells.2017.0151 (2017).
18. Kondo Y, Kanzawa T, Sawaya R, Kondo S, THE ROLE OF AUTOPHAGY IN CANCER DEVELOPMENT AND RESPONSE TO THERAPY. (2005) 10.1038/nrc1692.
19. Li J et al. Oxygen-sensitive methylation of ULK1 is required for hypoxia-induced autophagy. Nat Commun 13, (2022).
20. Mathew R et al. Autophagy suppresses tumor progression by limiting chromosomal instability. (2007) 10.1101/gad.1545107.
21. Mathew R, White E. Autophagy, stress, and cancer metabolism: What doesn't kill you makes you stronger. Cold Spring Harb Symp Quant Biol. 2011;76:389–96.
22. Lazova R, et al. Punctate LC3B expression is a common feature of solid tumors and associated with proliferation, metastasis, and poor outcome. Clin Cancer Res. 2012;18:370–9.
23. Hosokawa N et al. Nutrient-dependent mTORC1 Association with the ULK1-Atg13-FIP200 Complex Required for Autophagy. Mol Biol Cell 20, (1981).
24. Hwa Jung C et al. ULK-Atg13-FIP200 Complexes Mediate mTOR Signaling to the Autophagy Machinery. Mol Biol Cell 20, (1992).
25. Ganley IG, et al. ULK1·ATG13·FIP200 complex mediates mTOR signaling and is essential for autophagy. J Biol Chem. 2009;284:12297–305.
26. Neufeld TP. TOR-dependent control of autophagy: Biting the hand that feeds. *Current Opinion in Cell Biology* vol. 22 157–168 Preprint at https://doi.org/10.1016/j.ceb.2009.11.005 (2010).
27. Egan DF, Shackelford DB, Maria MM, Shaw RJ. Phosphorylation of ULK1 (hATG1) by AMP-activated protein kinase connects energy sensing to mitophagy. Science. 2011;331:456–61.

28. Correa RJM, Peart T, Valdes YR, Dimattia GE, Shepherd TG. Modulation of AKT activity is associated with reversible dormancy in ascites-derived epithelial ovarian cancer spheroids. Carcinogenesis. 2012;33:49–58.
29. Singha B. *Inhibiting ULK1 kinase decreases autophagy and cell viability in high-grade serous ovarian cancer spheroids*. *Am J Cancer Res* vol. 10 www.ajcr.us/ (2020).
30. Schindelin J et al. Fiji: An open-source platform for biological-image analysis. *Nature Methods* vol. 9 676–682 Preprint at https://doi.org/10.1038/nmeth.2019 (2012).
31. Arganda-Carreras I, et al. Trainable Weka Segmentation: A machine learning tool for microscopy pixel classification. Bioinformatics. 2017;33:2424–6.
32. Varghese F, Bukhari AB, Malhotra R, De A. IHC profiler: An open source plugin for the quantitative evaluation and automated scoring of immunohistochemistry images of human tissue samples. PLoS ONE 9, (2014).
33. Bjørkøy G, et al. *Chapter 1*2 Monitoring Autophagic Degradation of p62/SQSTM1. Methods Enzymol. 2009;452:181–97.
34. Kabeya Y, et al. The EMBO Journal – 2000 - Kabeya - LC3 a mammalian homologue of yeast Apg8p is localized in autophagosome membranes after. EMBO J. 2000;19:5720–8.
35. Shepherd TG, Dick FA. Principles of dormancy evident in high-grade serous ovarian cancer. *Cell Division* vol. 17 Preprint at https://doi.org/10.1186/s13008-022-00079-y (2022).
36. Kroeger PT, Drapkin R. Pathogenesis and heterogeneity of ovarian cancer. *Current Opinion in Obstetrics and Gynecology* vol. 29 26–34 Preprint at https://doi.org/10.1097/GCO.0000000000000340 (2017).
37. Demeter A et al. ULK1 and ULK2 are less redundant than previously thought: computational analysis uncovers distinct regulation and functions of these autophagy induction proteins. Sci Rep 10, (2020).
38. Zachari M, Ganley IG. The mammalian ULK1 complex and autophagy initiation. *Essays in Biochemistry* vol. 61 585–596 Preprint at https://doi.org/10.1042/EBC20170021 (2017).
39. Wheeler LJ et al. Multi-Omic Approaches Identify Metabolic and Autophagy Regulators Important in Ovarian Cancer Dissemination. *iScience* 19, 474–491 (2019).
40. Mizushima N. The role of the Atg1/ULK1 complex in autophagy regulation. *Current Opinion in Cell Biology* vol. 22 132–139 Preprint at https://doi.org/10.1016/j.ceb.2009.12.004 (2010).
41. Klionsky DJ et al. Guidelines for the use and interpretation of assays for monitoring autophagy (3rd edition). *Autophagy* vol. 12 1–222 Preprint at https://doi.org/10.1080/15548627.2015.1100356 (2016).
42. Tian W, et al. An antibody for analysis of autophagy induction. Nat Methods. 2020;17:232–9.
43. Wang C et al. Phosphorylation of ULK1 affects autophagosome fusion and links chaperone-mediated autophagy to macroautophagy. Nat Commun 9, (2018).
44. Russell RC, et al. ULK1 induces autophagy by phosphorylating Beclin-1 and activating VPS34 lipid kinase. Nat Cell Biol. 2013;15:741–50.

45. Menon MB, Dhamija S. Beclin 1 phosphorylation - at the center of autophagy regulation. *Frontiers in Cell and Developmental Biology* vol. 6 Preprint at https://doi.org/10.3389/fcell.2018.00137 (2018).
46. Correa RJM, Valdes YR, Shepherd TG, DiMattia GE. Beclin-1 expression is retained in high-grade serous ovarian cancer yet is not essential for autophagy induction in vitro. J Ovarian Res 8, (2015).
47. White E. Deconvoluting the context-dependent role for autophagy in cancer. Nat Rev Cancer. 2012. 10.1038/nrc3262.
48. Amaravadi RK et al. Principles and current strategies for targeting autophagy for cancer treatment. *Clinical Cancer Research* vol. 17 654–666 Preprint at https://doi.org/10.1158/1078-0432.CCR-10-2634 (2011).
49. Debnath J, Gammoh N, Ryan KM. Autophagy and autophagy-related pathways in cancer. *Nature Reviews Molecular Cell Biology* Preprint at https://doi.org/10.1038/s41580-023-00585-z (2023).
50. Yuan F, et al. ULK1 phosphorylates Mad1 to regulate spindle assembly checkpoint. Nucleic Acids Res. 2019;47:8096–110.
51. Joshi A, et al. Nuclear ULK1 promotes cell death in response to oxidative stress through PARP1. Cell Death Differ. 2016;23:216–30.
52. Wu W et al. The Autophagy-Initiating Kinase ULK1 Controls RIPK1-Mediated Cell Death. Cell Rep 31, (2020).
53. Xue ST, et al. The role of the key autophagy kinase ULK1 in hepatocellular carcinoma and its validation as a treatment target. Autophagy. 2020;16:1823–37.
54. Duan T, et al. ULK1 Depletion Protects Mice from Diethylnitrosamine-Induced Hepatocarcinogenesis by Promoting Apoptosis and Inhibiting Autophagy. J Hepatocell Carcinoma. 2023;10:315–25.
55. Deng R, et al. MAPK1/3 kinase-dependent ULK1 degradation attenuates mitophagy and promotes breast cancer bone metastasis. Autophagy. 2021;17:3011–29.
56. Quinn MCJ, et al. Identification of a locus near ULK1 associated with progression-free survival in ovarian cancer. Cancer Epidemiol Biomarkers Prev. 2021;30:1669–80.
57. Amaravadi RK, Kimmelman AC, Debnath J. Targeting autophagy in cancer: Recent advances and future directions. *Cancer Discovery* vol. 9 1167–1181 Preprint at https://doi.org/10.1158/2159-8290.CD-19-0292 (2019).

Figures

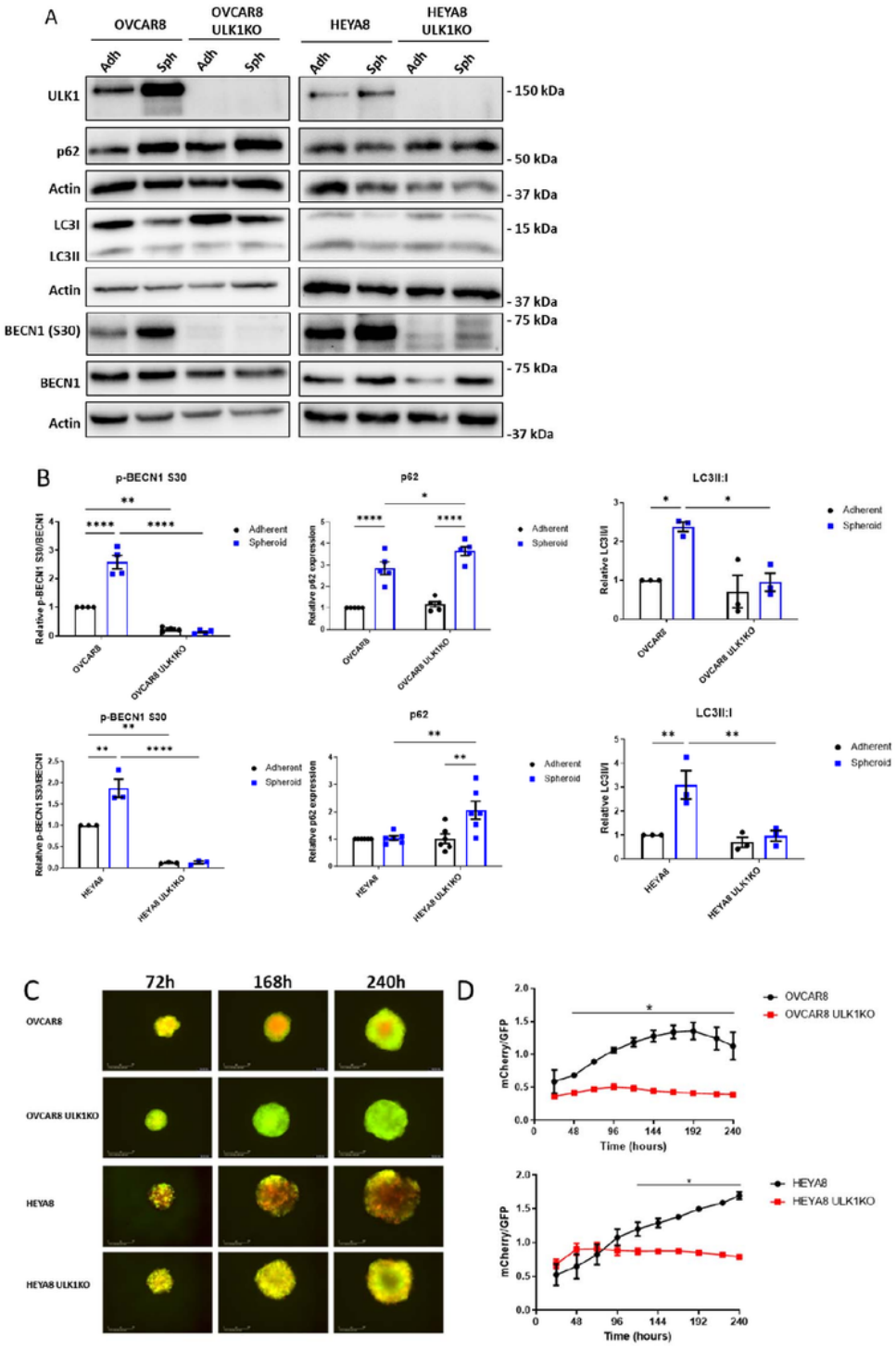

Figure 1

ULK1 is required for autophagy activation in EOC spheroids.

A) EOC (OVCAR8 and HEYA8) parental and *ULK1*KO cells were seeded in adherent and spheroid culture. Protein lysates were harvested 72h after seeding for western blot analysis for protein markers of autophagy and ULK1 activity. Full-length blots are presented in Supplementary File 1. B) Densitometric

analysis of p-Beclin1 (S30), p62, and LC3II:I expression in OVCAR8 and HEYA8 cells relative to expression in parental adherent conditions. Data displayed as mean ± SEM; Two-way ANOVA followed by Šidák's multiple comparisons test, *P<0.01, **P<0.001, ****P<0.0001. C) Fluorescent images of spheroids were captured across multiple days using the IncuCyte S3 Live-Cell Analysis System. D) Ratios of mCherry/GFP in mCherry-eGFP-LC3B spheroids are displayed as mean ± SEM (n=3); Multiple Student's *t*-test, *P<0.05.

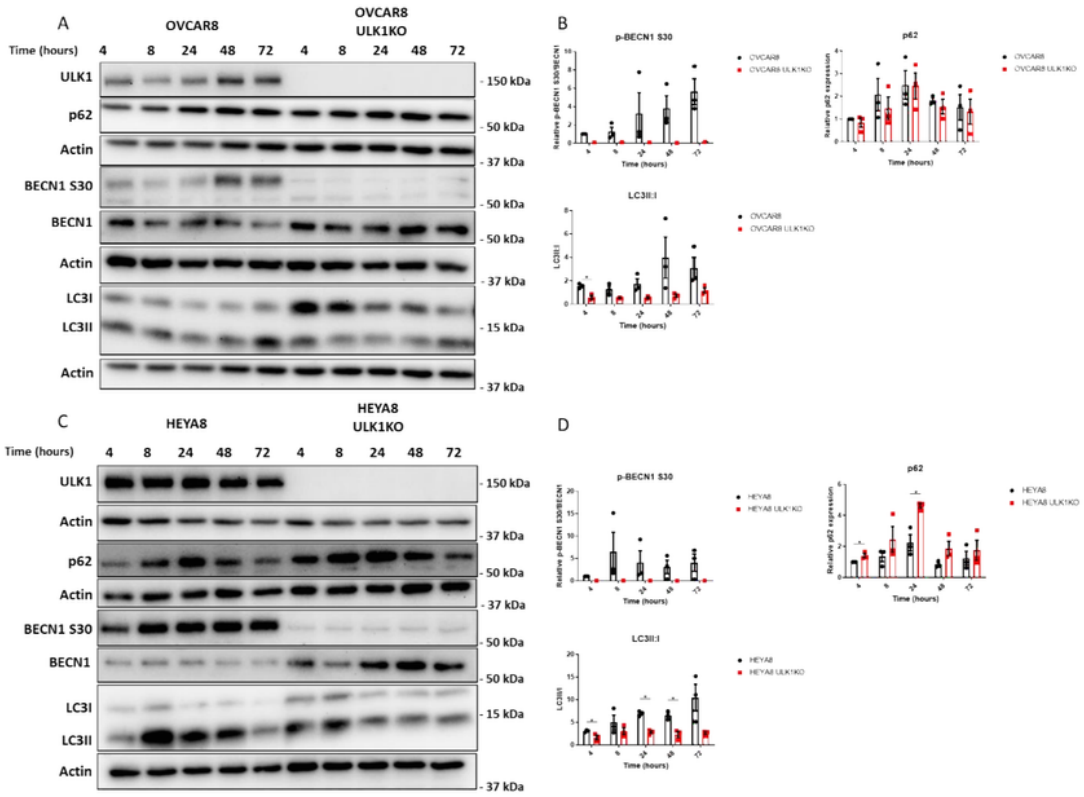

Figure 2

Autophagy activation is impaired early in EOC spheroid formation.

A) OVCAR8 parental and *ULK1*KO cells were seeded in spheroid culture and protein lysates were harvested 4, 8, 24, 48, and 72 hours after seeding for western blot analysis of protein markers of autophagy and ULK1 activity. Full-length blots are presented in Supplementary File 1. B) Densitometric analysis of p-Beclin1 (S30), p62, and LC3II:I expression (n=3) relative to expression in parental 4-hour spheroids. Data displayed as mean ± SEM; Multiple Student's *t*-test, *P<0.05.

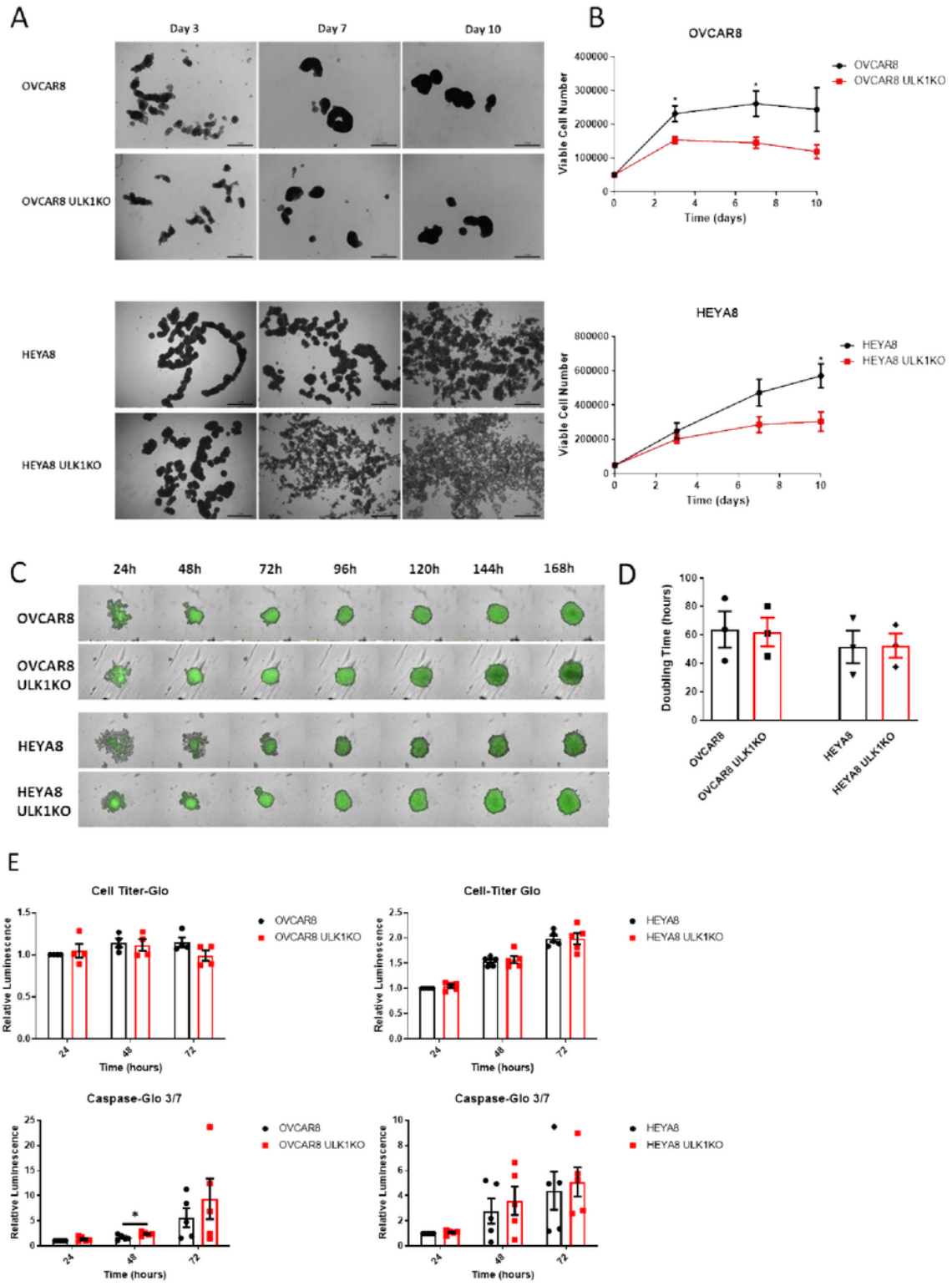

Figure 3

Viability is significantly impaired in EOC *ULK1*KO spheroids.

A) Brightfield microscopy images of EOC spheroids seeded in 24-well ULA plates. Images were captured at day 3, 7, and 10 using a Leica DMI 400B inverted microscope. Scale bar represents 1mm. B) Number of viable cells were counted using a Trypan Blue Exclusion Assay. Data displayed as mean ± SEM (OVCAR8

n=4, HEYA8 n=3); Student's *t*-test, *P<0.05. C) Fluorescent images of spheroids were captured across multiple days using the IncuCyte S3 Live-Cell Analysis System. D) Doubling time was a calculated on GraphPad Prism 9 using the Green Mean Intensity of GFP spheroids. E) Viability and apoptosis were measured using CellTiter-Glo and Caspase-Glo 3/7 luminescence assays, respectively. Cells were seeded at 2000 cells per well in a 96-well ULA plate. Data reflects luminescence relative to parental spheroids at 24-hours. Data displayed as mean ± SEM; Multiple Student's *t*-test, *P<0.05.

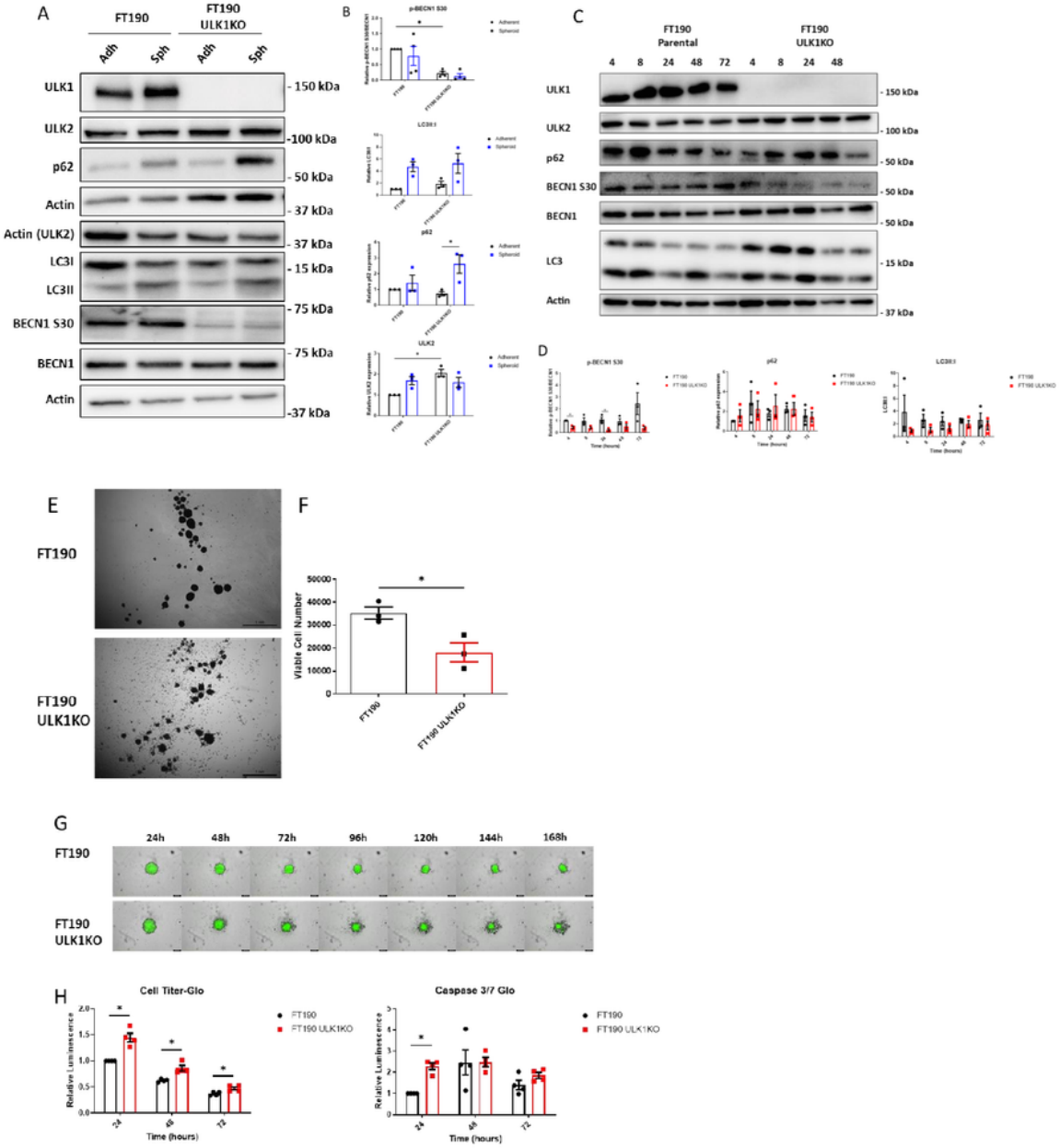

Figure 4

ULK1 is not required for autophagy activation in EOC precursor spheroids.

A) FT190 parental and *ULK1*KO cells were seeded in adherent and spheroid culture. Protein lysates were harvested 72h after seeding for western blot analysis for protein markers of autophagy and ULK1 activity. Full-length blots are presented in Supplementary File 1.B) Densitometric analysis of p-Beclin1 (S30), p62, and LC3II:I expression in FT190 cells (n=3) relative to parental cell adherent culture conditions. Data displayed as mean ± SEM; Two-way ANOVA followed by Šidák's multiple comparisons test, *P<0.01, **P<0.001, ****P<0.0001. C) FT190 parental and *ULK1*KO cells were seeded in spheroid culture and protein lysates were harvested 4, 8, 24, 48, and 72 hours after seeding for western blot analysis of protein markers of autophagy and ULK1 activity. Full-length blots are presented in Supplementary File 1. D) Densitometric analysis of p-Beclin1 (S30), p62, and LC3II:I expression (n=3) relative to parental cell 4-hour spheroids. Data displayed as mean ± SEM; Student's *t*-test, *P<0.05. E) Brightfield microscopy images of EOC spheroids seeded in 24-well ULA plates. Images were captured at day 3, 7, and 10 using a Leica DMI 400B inverted microscope. Scale bar represents 1mm. F) Number of viable cells were counted using a Trypan Blue Exclusion Assay. Data displayed as mean ± SEM (n=3); Student's *t*-test, *P<0.05. G) Fluorescent images of spheroids were captured across multiple days using the IncuCyte S3 Live-Cell Analysis System. H) Viability and apoptosis were measured using CellTiter-Glo and Caspase-Glo 3/7 luminescence assays, respectively. Data reflects luminescence relative to parental spheroids at 24-hours. Data displayed as mean ± SEM (n=4); Student's *t*-test, *P<0.05.

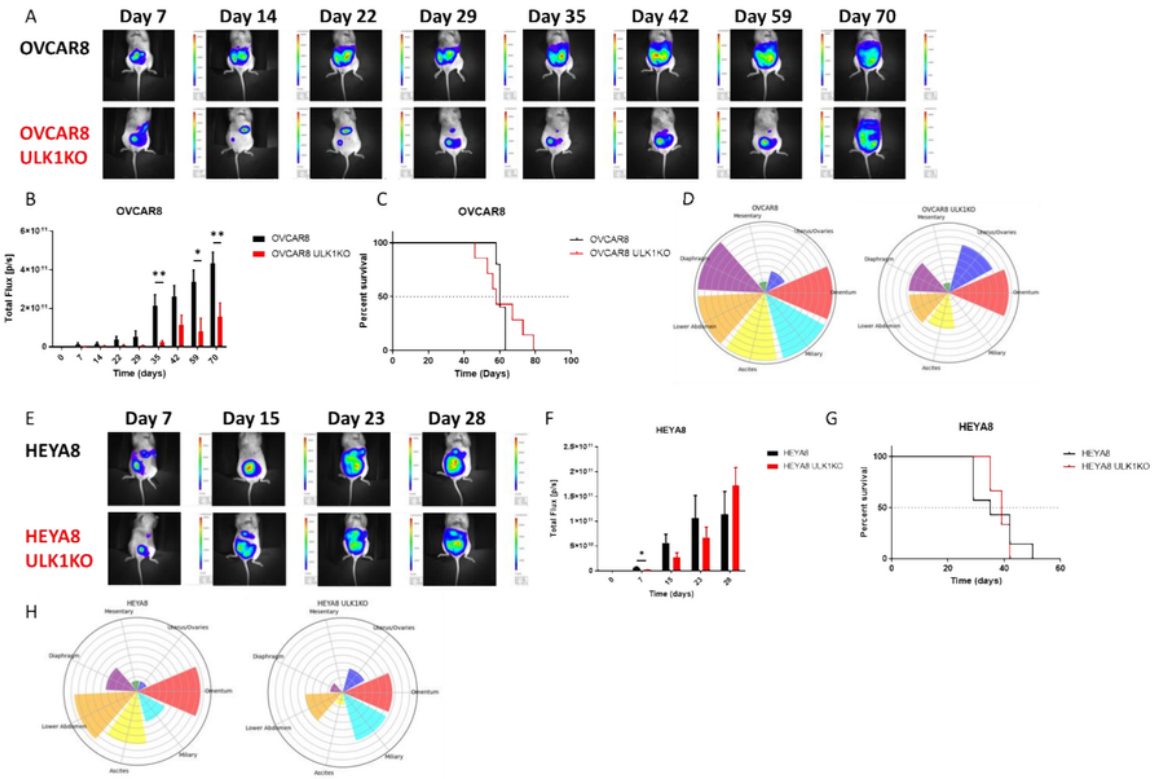

Figure 5

ULK1 affects both initial and advanced phases of tumor development in xenograft models

A/E) Representative bioluminescent images of tumor burden in mice injected i.p with OVCAR8 and HEYA8 parental and *ULK1*KO cells (n=8 each). B/E) Total flux (p/s) was used as measure of tumor burden. Mice were injected with luciferin and tumor burden was assessed via bioluminescence imaging weekly. C/G)

Kaplan-Meier survival analysis shows the overall survival (in days) of mice injected with EOC parental and *ULK1*KO cells. Dotted line reflects median survival (OVCAR8 parental; 61.5d, *ULK1*KO; 57d, HEYA8 parental; 38d, *ULK1*KO; 40d). D/H) Petal plots representing the proportion of mice displaying tumors at numerous peritoneal sites as indicated. Radial gridlines represent 10% gradations (OVCAR8; n=6, OVCAR8 *ULK1*KO; n=7, HEYA8; n=7, HEYA8 *ULK1*KO; n=6).

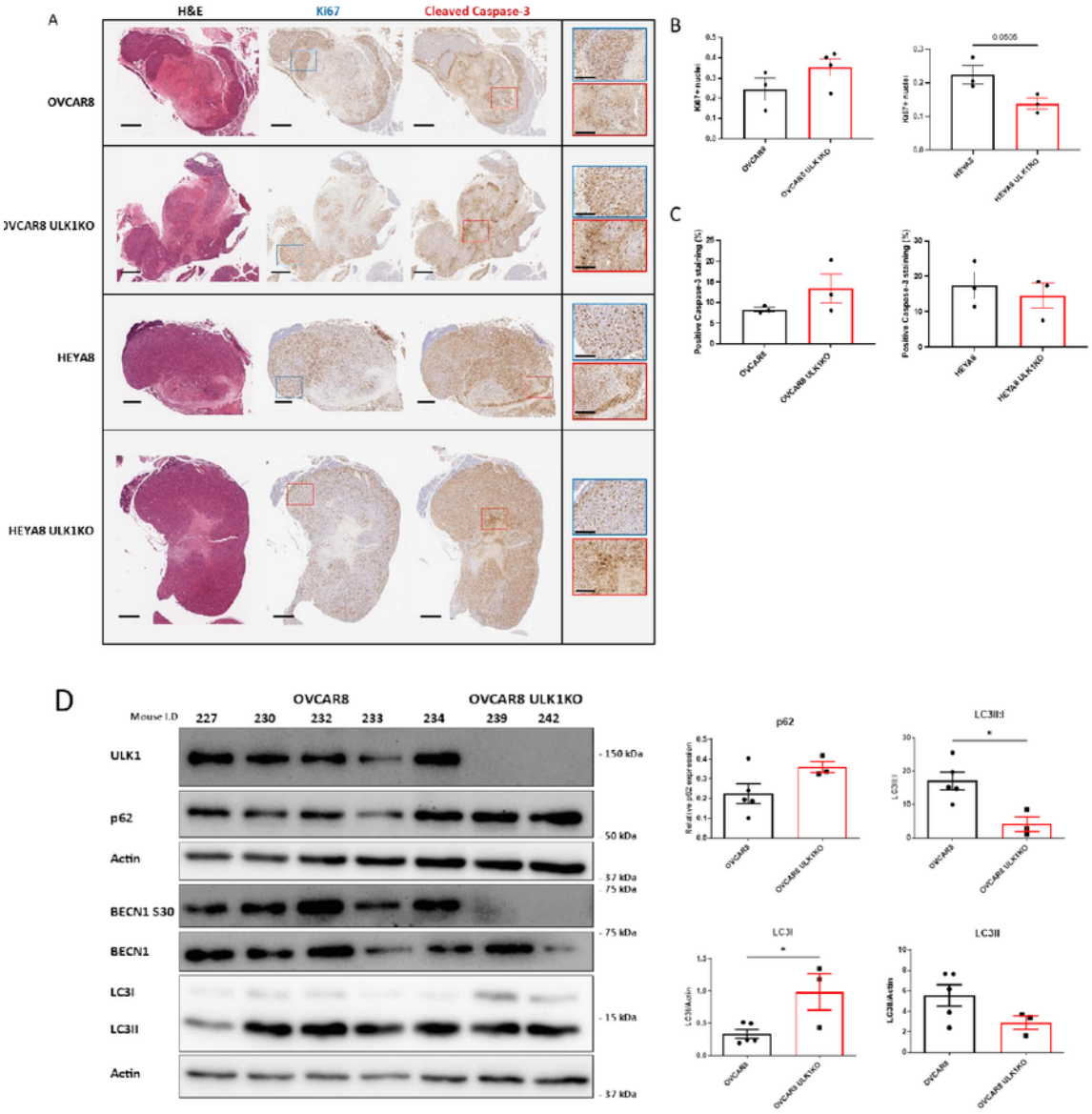

Figure 6

Histopathologic differences due to ULK1 loss in xenografted EOC tumors.

A) Serial sections were stained with hematoxylin and eosin (H&E), and immunostained using Ki67 for proliferation and cleaved caspase-3 for apoptosis. Scale bar: large section, 600 mm; high magnification section, 200 mm.B) Quantification of Ki67 staining. Data displayed as mean number of Ki67 positive nuclei for each tumor and the overall mean. For every group, Ki67 positivity was assessed in at least three independent tumors. Data displayed as mean ± SEM; Student's *t*-test. C) Quantification of cleaved caspase-3 staining. Data displayed as mean percent of positive cleaved caspase-3 staining for each tumor and the overall mean. For every group, cleaved caspase-3 positivity was assessed in at least three independent tumors. Data displayed as mean ± SEM; Student's *t*-test. D) Western blot and densitometric analysis of p62, LCII:I, LCI, and LC3II in spheroid culture from cells derived from ascites in OVCAR8 xenografts. Data displayed as mean ± SEM (OVCAR8; n=5, OVCAR8 *ULK1*KO; n=3); Student's *t*-test, *P<0.05. Full-length blots are presented in Supplementary File 1.

Supplementary Files

This is a list of supplementary files associated with this preprint. Click to download.

- SUPPLEMENTALFIGURELEGENDS.pdf
- SupplementalFiguresFinal.pdf
- SupplementalFile1.pdf